Journal of Biomedical Optics

SPIEDigitalLibrary.org/jbo

Actin restructuring during *Salmonella typhimurium* infection investigated by confocal and super-resolution microscopy

Jason J. Han
Yuliya A. Kunde
Elizabeth Hong-Geller
James H. Werner

SPIE

Actin restructuring during *Salmonella typhimurium* infection investigated by confocal and super-resolution microscopy

Jason J. Han,[a] Yuliya A. Kunde,[b] Elizabeth Hong-Geller,[b] and James H. Werner[a,*]
[a]Los Alamos National Laboratory, Center for Integrated Nanotechnologies, Los Alamos, New Mexico 87545
[b]Los Alamos National Laboratory, Biosciences Division, Los Alamos, New Mexico 87545

Abstract. We have used super-resolution optical microscopy and confocal microscopy to visualize the cytoskeletal restructuring of HeLa cells that accompanies and enables *Salmonella typhimurium* internalization. Herein, we report the use of confocal microscopy to verify and explore infection conditions that would be compatible with super-resolution optical microscopy, using Alexa-488 labeled phalloidin to stain the actin cytoskeletal network. While it is well known that actin restructuring and cytoskeletal rearrangements often accompany and assist in bacterial infection, most studies have employed conventional diffraction-limited fluorescence microscopy to explore these changes. Here we show that the superior spatial resolution provided by single-molecule localization methods (such as direct stochastic optical reconstruction microscopy) enables more precise visualization of the nanoscale changes in the actin cytoskeleton that accompany bacterial infection. In particular, we found that a thin (100-nm) ring of actin often surrounds an invading bacteria 10 to 20 min postinfection, with this ring being transitory in nature. We estimate that a few hundred monofilaments of actin surround the *S. typhimurium* in this heretofore unreported bacterial internalization intermediate. [DOI: 10.1117/1.JBO.19.1.016011]

Keywords: super-resolution; fluorescence microscopy; host-pathogen; bacteria; protein.

Paper 130691RR received Sep. 23, 2013; revised manuscript received Dec. 12, 2013; accepted for publication Dec. 13, 2013; published online Jan. 10, 2014.

1 Introduction

Over the past few decades, a number of far-field super-resolution (SR) optical microscopies have been developed that enable fluorescence imaging of cellular structure with unprecedented subdiffraction-limited spatial resolution.[1–8] The three primary SR optical configurations are stimulated emission depletion (STED) microscopy,[8] which is a confocal scanning–based technique that achieves resolution enhancement by limiting the spatial distribution of excited fluorophores in the sample; structured illumination microscopy (SIM),[5] which uses patterned, or structured, light to encode normally inaccessible high-spatial frequency information into the fluorescence signal; and single-molecule localization microscopy (SMLM),[1–3] which relies on high-precision centroid localization of spatially isolated single-point emitters. Each technique presents strengths and weaknesses with respect to spatial and temporal resolution, sample preparation requirements, three-dimensional (3-D) optical sectioning capabilities, and instrument complexity. For example, both STED (Ref. 9) and SIM (Ref. 10) may offer faster temporal resolution and greater 3-D optical sectioning than SMLM. In contrast, single-molecule localization methods afford the best lateral spatial resolution with the simplest experimental setup.

SMLM is a wide-field CCD-based imaging technique that achieves SR by precise centroid localization of spatially isolated single fluorescent emitters. Although several variations and acronyms, such as photo-activation localization microscopy (PALM) (Ref. 1), stochastic optical reconstruction microscopy (STORM) (Ref. 3), fluorescence PALM (F-PALM) (Ref. 2), or direct STORM (dSTORM) (Ref. 11) exist, the unifying theme that has enabled all SMLM methods is the ability to photophysically switch a fluorescent dye molecule between a nonemissive "off" (dark) state in which fluorescence is suppressed and an emissive "on" (bright) state in which normal fluorescence occurs. More importantly, for a densely labeled sample, the relative number of molecules in the bright (Nbright) and dark (Ndark) states must be carefully controlled and maintained such that Nbright $\ll$ Ndark during the entire course of the imaging experiment. This requirement is due to the fact that in SMLM, it is essential that molecules are imaged individually, such that in any given image, the point spread function of two molecules in the bright state are not overlapped. In SMLM, individual molecules are localized with high precision (typically 10 to 20 nm, limited by the total number of photons detected and background noise[12]), with a computer-generated image of all centroids detected during the course of the experiment being used to construct a high-resolution map of the underlying molecular density of the fluorophore used for fluorescent labeling.

Over the course of evolution of SR imaging methods, the cytoskeleton has been a common model target for both static and dynamic SR imaging because long, one-dimensional structural elements (i.e., filaments and microtubules) can be selectively labeled in a low background environment, thereby providing excellent image contrast.[13,14] While other nonoptical modes of imaging, such as high-resolution scanning electron microscopy, have been utilized to image exposed actin filaments with near atomic resolution,[15] the actin cytoskeleton in whole

*Address all correspondence to: James H. Werner, E-mail: jwerner@lanl.gov

fixed or living cells cannot, in general, be easily imaged by SEM methods since the plasma membrane is typically coated with a metal to provide image contrast. Transmission electron microscopy (TEM) combined with ultrathin sectioning and immunostaining does provide the ability to reconstruct the entire actin cytoskeleton of fixed, embedded cells in three dimensions, but at the cost of tedious sample preparation that requires a substantial amount of time and expertise. Given the strengths of SR optical microscopy for imaging actin structure in live and fixed cells, it would be of great interest to exploit SR methods to examine changes in actin structure that accompany various phases of cell life and fate.

In particular, rearrangements in the actin cytoskeleton are a vital component of many bacterial infections.[16,17] In healthy cells, polymerization and depolymerization between monomeric g-actin and polymeric f-actin is tightly regulated both spatially and temporally through a complex interplay of several known, and likely yet-to-be-discovered, signaling, scaffolding, and actin-binding proteins.[18,19] For bacteria to invade a host cell, this regulation must be disrupted and controlled. To this end, many bacteria have evolved novel methods to regulate host cytoskeletal structure and dynamics. One highly conserved bacterial mechanism of manipulating host cell signaling and actin dynamics is the type III secretion system (T3SS), a needle-like sensory appendage utilized by several pathogenic species of gram-negative bacteria (e.g., *Shigella*, *Salmonella*, *E. coli*, and *Yersinia*)[20,21] to inject bacterial effector proteins into the host cell.

The bacterium *Salmonella typhimurium* is a prime example of bacterial control of host cytoskeleton structure. *S. typhimurium* is a pathogenic gram-negative bacterium that causes gastroenteritis in humans and other mammals.[22] The infection mechanism of *S. typhimurium* is well documented.[20,22,23] Upon first contact with a host epithelial cell, specific host cell receptors aggregate at the point of physical contact, with *S. typhimurium* injecting a number of bacterial effector proteins into the host cell via the T3SS. Once inside the cell, specific bacterial effectors (e.g., SopE) restructure actin dynamics at the site of infection by polymerizing g-actin into branch-like f-actin extensions.[16,24,25] As actin extensions elongate, membrane ruffles form and surround the invading bacterium until the prokaryotic intruder is completely engulfed. Ultimately, the pathogen is internalized into the host cell as a modified phagosome, termed the *Salmonella*-containing vacuole (SCV), where the pathogen replicates inside the host cell to propagate infection. The infection process is known to occur rapidly within minutes of first contact of the host cell, with cytoskeletal rearrangements occurring in HeLa cells ~20 min after infection and dissipating over the course of an hour.[17,26]

The biochemical interactions between T3SS bacterial effector proteins and host cell regulatory proteins during infection have been extensively studied in several pathogens, including *Listeria*, *Yersinia*, and *Burkholderia*.[27] These studies have elucidated several specific host cell proteins targeted by T3SS bacterial effectors. However, because such studies are typically conducted using nonimaging molecular biology methods, they do not, in general, provide spatial information. In contrast, fluorescence microscopy has been utilized to image host cell receptor aggregation during infection,[23] bacterial effector injection and localization,[21,28] and actin restructuring[29] in both fixed and living cells. These imaging studies have focused on facilitating our understanding of the spatial relationship between host cell and bacterial constituents during the infection process. TEM has also been utilized to capture an extracellular bird's-eye view of the various stages of infection, providing molecular details of membrane ruffling and bacterial entry into the host cell at spatial resolutions unobtainable by conventional optical microscopy.[30] These imaging efforts underscore the interest in, and importance of, visualizing the spatial relationship between the host cell and bacterial components that participate in the infection process and emphasize the need to continually employ new and emerging imaging technologies to gain further insight into the specific spatial details of the infection process, as well as cellular structure in general. With SR imaging microscopes that are now commercially available or readily obtainable through custom modifications of existing microscopes, imaging of cellular structure during events such as bacterial infection can be revisited beyond the diffraction limit, with the aim of furthering knowledge of such events.

In this work, we aim to better understand the nanometer-level spatial relationship between localized host cell actin cytoskeleton restructuring and the invading bacterium by employing SMLM. Here we show that more precise measurements of actin restructuring (such as quantifying the number of actin monofilaments surrounding an invading bacteria) are possible with single molecule-based SR imaging when compared to conventional fluorescence microscopy. We demonstrate that single molecule-based SR imaging is a powerful method that complements existing methods for the visualization and study of bacterial infection due to its molecular specificity, compatibility with conventional optical microscopy, and superior spatial resolution.

2 Materials and Methods

2.1 *Growth of HeLa Cells and S. typhimurium*

HeLa cells (ATCC-CCL2) were cultured in Dulbecco's modified Eagle's medium (Invitrogen, Carlsbad, California) supplemented with 10% fetal bovine serum, 2 mM glutamine, and 1 mM sodium pyruvate at 37°C and 5% CO_2. Wild-type *S. typhimurium* (SB300, gift of Jorge Galan, Yale School of Medicine) was propagated in lysongeny broth and streptomycin (50 μg/ml) with shaking at 155 rpm at 37°C.

2.2 *Infection Protocol*

HeLa cells were seeded on eight-chamber borosilicate glass bottom slides (NUNC 1554111) at a density of 1.3×10^4 cells/well the day before infection and determined to grow to 2×10^4 cells/well overnight. An overnight culture of *S. typhimurium* was diluted about fivefold and regrown to ~10^8 cells/ml, and bacterial density was calculated using a spectrophotometer. Slides of HeLa cells were infected at a multiplicity of infection (MOI) of 0, 20, and 40 and centrifuged for 5 min at 500 rpm to initiate host-pathogen contact. Slides were then placed at 37°C, 5% CO_2. One slide containing uninfected cells to act as a $t = 0$ control was immediately processed by washing three times with phosphate-buffered saline (PBS), fixation in 3.7% formaldehyde for 20 min at room temperature, and three more washes in PBS. After 5, 10, 20, and 30 min of incubation at 37°C, slides containing infected HeLa cells at different MOIs were also fixed as described.

2.3 *Staining Protocol*

All fixed cells were then permeabilized with 0.01% Triton X-100 in PBS for 10 min at room temperature and washed three times with PBS. To block nonspecific binding of dye to the slide, a 5% bovine serum albumin (BSA) solution in PBS was added to each well for 30 min and the cells were washed three times with PBS. To stain actin, cells were labeled with 2.5 μl of a 6.6-μM stock solution of Alexa Fluor 488 phalloidin (Invitrogen) in 100 ml PBS/1% BSA solution for 30 min at room temperature in the dark. To stain *S. typhimurium*, cells were labeled with a mouse anti-*Salmonella* lipopoylysaccharide (LPS) antibody 1E6 (ThermoFisher, Waltham, Massachusetts) at a final concentration of 3 μg/ml in PBS/1% BSA for 1 h in the dark. Cell samples were incubated with a goat anti-mouse Alexa Fluor 568 (Invitrogen) secondary antibody reagent at 3 μg/ml in PBS/1% BSA for 1 h in the dark and then washed three times with PBS, prior to imaging.

2.4 *Confocal Imaging*

Confocal images and Z scans (using 100-nm steps) were obtained on an Olympus Fluoview microscope using a 60× 1.2 NA water immersion objective. Excitation for the Alexa-488-labeled phalloidin was provided by ~5 μW of 488-nm excitation (Sapphire Laser, Coherent, Santa Clara, California), whereas the Alexa-568-labeled secondary antibody against the mouse monoclonal anti-LPS was excited by 10 μW of 532-nm excitation provided by an Nd:YAG (CrystaLaser, Reno, Nevada). Fluorescence emission was split using a 570-nm long-pass dichroic mirror with the reflected and transmitted light focused onto two photomultiplier tube channels of the microscope. Channel 1 employed a BA505-525 band-pass filter (for Alexa-488 detection), whereas channel 2 used a band-pass filter centered at 605 nm (for Alexa-568 detection). All filters were acquired from Olympus (Center Valley, Pennsylvania). All confocal microscopy images were deconvolved using Huygens Essential version 3.7 (SVI Imaging, Hilversum, The Netherlands). XY, YZ, and XZ maximum intensity projection images from the same Z-scan series were combined into single cubic representations shown.

2.5 *Single-Molecule Localization: Microscope*

Figure 1 depicts a schematic of our SR microscope, which was built around an Olympus IX71 inverted base and equipped with multiple laser lines and shutters to accommodate PALM, STORM, and dSTORM imaging modes. A solid-state violet laser (405 nm, CrystaLaser), sapphire blue laser (488 nm, Coherent), and diode-pumped green laser (561 nm, CrystaLaser) were coaligned using appropriate dichroic beamsplitters (Semrock LM01-427 and LM01-503, Rochester, New York). As illustrated for the 488-nm laser, the collimated excitation beam was directed by a multilaser line excitation dichroic (Semrock Di01 R405/488/561/635) and focused onto the back aperture of a 1.49 NA 60× oil-immersion objective (Olympus). In order to preferentially excite restructuring actin several microns away from the cover glass surface, we utilized Hi-Lo microscopy,[31] which reduces background considerably compared to epi-excitation. This was achieved by translating the 488-nm laser toward, but not to, the critical angle required for total internal reflection (TIR). Since TIR conditions were not met, the excitation beam exited the objective at a very low angle. The final angle of the outgoing beam was fine tuned for each sample to maximize the signal-to-noise ratio. Fluorescence emission was collected through the same objective, spectrally filtered, and then focused onto the active area of an electron-multiplying (EM) CCD camera (Princeton Instruments, Trenton, New Jersey) Pro-EM, 512 × 512 pixels). For these experiments, the standard tube lens was removed from the microscope and a 450-mm achromat (Edmund Optics 49-282, Barrington, New Jersey) was used in its place. The objective-achromat optical relay resulted in a total magnification of

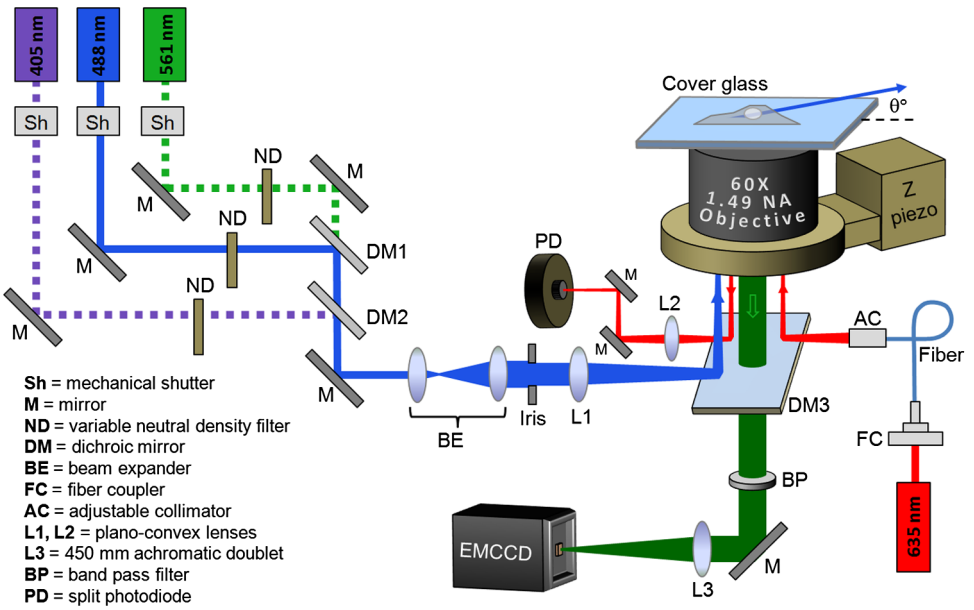

Fig. 1 Schematic of the single-molecule localization microscope used in this study. Hi-Lo microscopy using a 488-nm laser beam was used for fluorescence excitation, with the microscope Z position held constant by a home-constructed autofocus system that employed a red (635-nm) diode laser, a split photodiode, and a Z-piezo mount for the objective.

150× and mapped each pixel of the EM-CCD onto a 106 × 106-nm area in sample space, with this pixel size chosen to optimize localization precision following the estimates of Thompson et al.[12] To eliminate Z-drift during image acquisition, we employed a custom autofocus module that used a 635-nm diode laser beam (Thorlabs LDM635, Newton, New Jersey) sent into the microscope in through-objective TIR mode on the opposite side of the objective from the 488-nm excitation beam. The returning 635-nm beam was focused onto the active area of a split photodiode and the voltage outputs were sent into a PCI I/O board (National Instruments, Austin, Texas) and used as inputs to a proportional-integral-differential (PID) feedback loop that adjusted the Z position of the objective through a piezo controlled microscope objective mount (P-725 PIFOC, Physik Instrumente, Auburn, Massachusetts). The goal of the PID feedback loop was to keep the voltages on the split photodiode equal, thus maintaining a constant focus on the EM-CCD camera during image acquisition. The entire instrument (shutters, EM-CCD acquisition, Z autofocus system) was controlled and automated using custom LabVIEW programs.

2.6 *Single-Molecule Localization: Acquisition*

Our image acquisition and dye activation procedure closely followed the dSTORM protocol developed by Sauer and coworkers.[11] For fluorescence excitation of Alexa-488 dyes, we utilized 488-nm laser powers up to 50 mW (as measured coming out of the objective) spread over a 30-μm-diameter illumination area, corresponding to a radiative flux of up to ~5 kW/cm^2. Under these excitation powers, we found that the majority of Alexa-488 dyes could be driven and maintained in a light-induced dark state without adding reducing agents to the buffer employed (PBS, pH 7.4). As a result, a small number (10 to 50) of molecules were in a fluorescent state inside the field of view used for imaging [typically a 20 × 20-μm region of interest (ROI)]. Alexa 488 fluorescence emission was spectrally filtered (Semrock FF01-520/35 band-pass filter) before being focused onto the EM-CCD. Images were acquired at a frame rate of 20 Hz using 50-ms exposure time. Typically, 100 frames were collected and written to disk while acquiring the next 100 frames. A total of 300 to 500 cycles of 100 frames were acquired with an EM gain of 100. In order to minimize XY drift, the sample was allowed to settle on microscope stage for 10 to 20 min prior to imaging. Prior to SMLM, wide-field white light images of cells were obtained, followed by conventional epi-fluorescence imaging using 488-nm light combined with the FF01-520/35 filter for imaging the Alexa-488 labeled phalloidin. Conventional epi-fluorescence imaging of *Salmonella* was performed using low-power (~1 mW) 561-nm excitation combined with an FF01-593/40 emission filter (Semrock).

2.7 *Single-Molecule Localization: Processing*

Analysis was performed frame by frame for the single-molecule localization images. For each frame in the image acquisition, the average dark counts were subtracted from each image, followed by converting measured analog to digital units to photons using a manufacturer-provided specification sheet. A binary image was then formed, with the threshold value for the binary mapping typically chosen to be 3 standard deviations above mean pixel value. The centroid values of the contiguous areas of the binary images are calculated with these positions used as starting points to calculate centroid coordinates for the nonthresholded image using a 5 × 5 pixel grid centered on the centroids found in the binary image. Spots and centroids are found in this manner for all frames in the single-molecule image acquisition. The pixel intensity values for spots lasting multiple frames were summed if their centroid positions were <1.5 pixels apart. Single-molecule spots that disappeared for three consecutive frames were considered as bleached, and any new spot appearing thereafter in the same pixel grid was counted as a new molecule. After adding image frames for those molecules/spots that appeared in successive frames, images of individual spots were cross-correlated with a calculated point spread function. Only spots with a cross-correlation coefficient >0.8 and a summed intensity for the 5 × 5 pixel box surrounding the centroid exceeding 200 photons were then fitted to a two-dimensional (2-D) Gaussian using nonlinear least squares fitting, with an average molecule used in the SR image emitting ~3000 photons before bleaching. SR images were constructed by plotting a Gaussian for each molecule/spot found, with the width of the Gaussian spot plotted equal to the standard error of the fit, following the procedures laid forth by Betzig et al.[1] We note that while maximum likelihood methods of single-molecule localization can have greater accuracy than least-squares fitting procedures,[32] least-squares methods are faster computationally, which is the primary reason they were implemented here (though we note that GPU-based localization methods have greatly increased the speed of maximum likelihood methods[33]). The standard error of the fit obtained in our single-molecule data is, on average, larger (by a factor of 1.5) than the theoretical estimates of Thompson[12] and slightly larger (by a factor of 1.2) than the error expected when the excess noise factor of the EM-CCD is taken into account (following the estimates of Mortensen[32]). All SR images rendered here are displayed using 5-nm pixels. All fitting and data analysis was performed using custom software written in Igor Pro (Wavemetrics, Eugene, OR).

3 Results

Prior to SMLM of *S. typhimurium* infection, we used standard confocal fluorescence microscopy to quickly assess infection scenarios for which to apply superior single-molecule localization imaging. In particular, we note that while there has been some progress in extending SMLM methods from 2-D to 3-D,[13,34] many of these methods are limited in their depth of field to ±500 nm[13] or are equipment intensive.[34] Due to the degradation in localization precision that comes from having a high background,[12] SMLM is generally better suited to looking at thin samples (such that they can be imaged by through-objective TIR microscopy[35] or Hi-Lo microscopy[31]) to minimize the background and increase the localization precision. As such, conventional confocal microscopy was used to verify infection scenarios in which internalized bacteria could often be found only a few micrometers away from the coverslip-host cell interface.

Figure 2 shows confocal microscopy scans of actin-labeled HeLa cells fixed 10, 20, and 30 min following infection by *S. tymphimurium*. At each time point, invading bacteria are observed at progressively deeper depths within the restructuring actin. At 10 min postinfection [Fig. 2(b)], the process of internalization is fully underway as restructuring actin begins to surround and pull in the invading bacteria. At 20 min postinfection [Fig. 2(c)], bacteria have penetrated deeper into the host cell and are more entangled in the restructured actin cytoskeleton. By

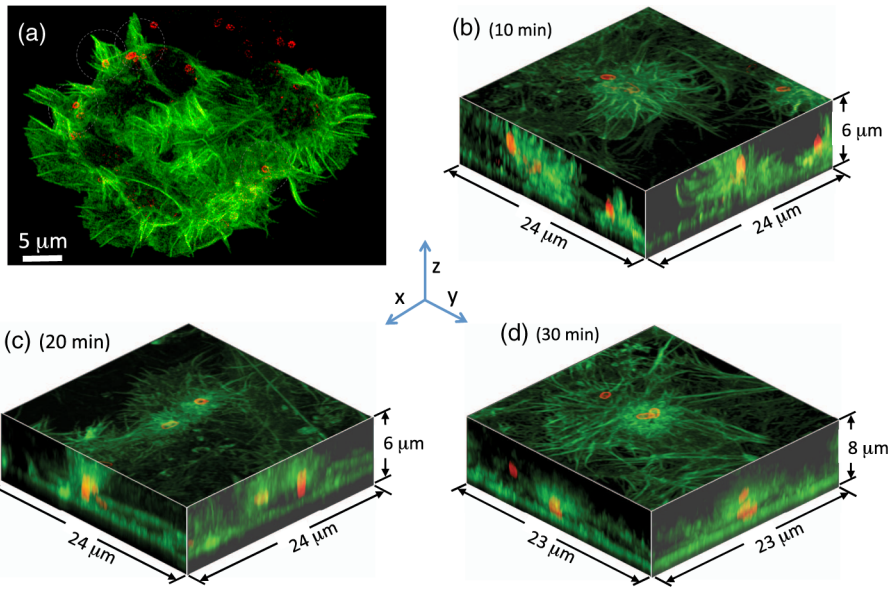

Fig. 2 Confocal fluorescence microscopy images of the actin cytoskeleton of HeLa cells at fixed time points following infection with *S. typhimurium*. Actin is shown in green (via an Alexa 488 phalloidin stain), whereas the *S. typhimurium* is red (Alexa-568 secondary antibody against an anti-LPS mouse monoclonal). (a) XY image of a single HeLa cell showing multiple cytoskeletal restructuring sites during the infection and internalization process 10 min postinfection. XYZ volumetric representations of HeLa cells (b) 10 min, (c) 20 min, and (d) 30 min postinfection show the progression of internalization.

30 min postinfection, bacteria appear to be fully engulfed in restructured actin, and maturation into an SCV is most likely the next step in the infection process. Interestingly, on a few occasions, we observed two bacteria colocalized within the same infection site, as shown in Fig. 2(d). The presence of two bacteria within the same entangled mass of restructuring actin suggests that both bacteria may have entered the cell through the same infection site, with the first bacterium potentially providing a preferred environment for the second entry. These confocal fluorescence images confirm the key role actin restructuring plays in bacterial entry and suggest that times of 10 to 20 min postinfection are ideal for SR imaging of the initial stages of internalization in HeLa cells.[17]

After establishing infection conditions compatible with SMLM, we commenced with SR imaging of *S. typhimurium*-induced actin restructuring at fixed time intervals postinfection. Figure 3(b) shows one such single-molecule localization SR image compared to a diffraction-limited image obtained by conventional epi-fluorescence imaging [Fig. 3(a)]. Figure 3(c) compares line scans across one of the more prominent actin features in Figs. 3(a) and 3(b) in the vicinity of a phagocytosing bacteria that is likely to have undergone dynamic rearrangement during bacterial internalization. We note that at normal optical resolutions [Fig. 3(c), top], there appear to be only two large actin bundles present in this ROI. In contrast, the superior resolution provided by the single-molecule localization image [Fig. 3(c), bottom] clearly shows that one of the bundles is formed from two smaller ones. We emphasize that the gnarled and highly entangled actin structures shown in Fig. 3 result from dramatic changes in the host cytoskeleton resulting from bacterial infection. Normal, noninfected HeLa cells have long, straight cytoskeletal features [as shown in Figs. 4 and 2(a) for actin not close to an infection site].

Due to the extensive cytoskeletal rearrangements that occur during bacterial infection, morphological changes at the site of

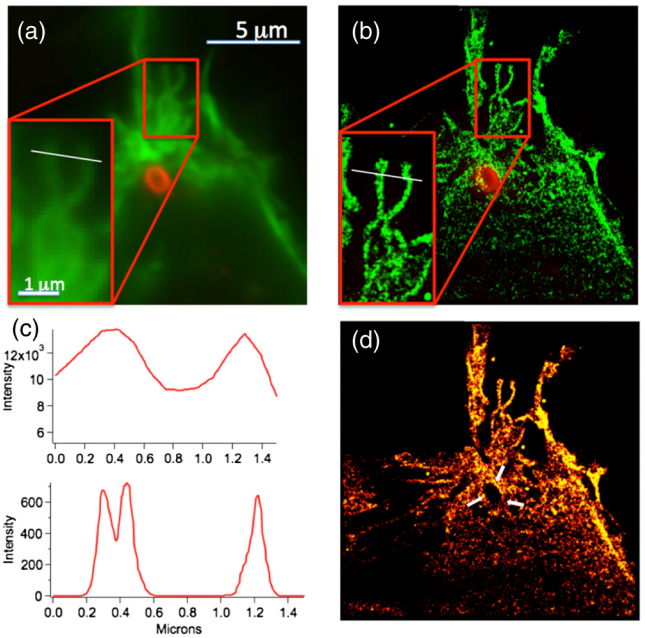

Fig. 3 Comparison of conventional and single-molecule localization images of actin restructuring during *Salmonella* infection. (a) Overlay of the actin cytoskeleton (green) and *Salmonella* (red) as observed by conventional epi-fluorescence microscopy. Blow up in lower left features a selected region of the actin cytoskeleton. (b) Overlay of the *Salmonella* (red) obtained with conventional microscopy with the actin cytoskeleton imaged by single-molecule localization microscopy (green). (c) Line scans through a selected region of the cytoskeleton from the normal resolution image (top) and single-molecule localization image (bottom). The region of these line scans are denoted by the white lines shown in the blown-up region of (a) and (b). (d) Single-molecule localization micrograph shown in a flame scale without the actin overlay. Note that the bacterial site (highlighted by white arrows) is evident by the void region in the actin cytoskeleton and that a thin ring of actin appears to be associated with the internalized bacteria.

infection are occasionally visible with white light illumination [Fig. 5(a)]. Figures 5(b) and 5(c) show corresponding diffraction-limited and SR images, respectively, of the actin network in an ROI encompassing the primary infection site shown in Fig. 5(a), with the bacteria overlaid in red. Figure 5(d) shows the SMLM image without the bacteria overlay.

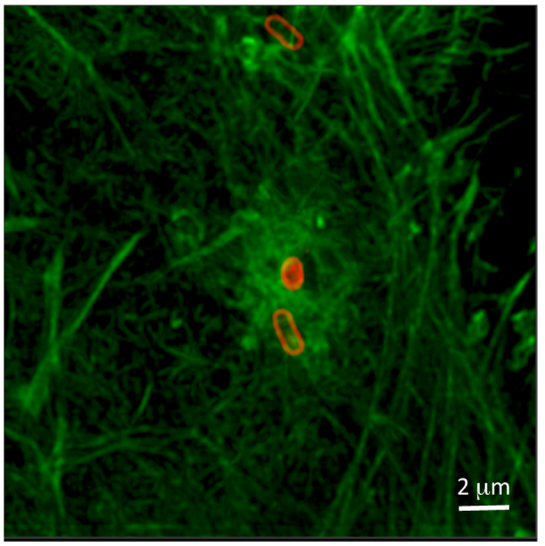

Fig. 4 Confocal micrograph of actin restructuring during *S. typhimurium* infection. Note the highly entangled and gnarled actin at the site of infection and the straight cytoskeletal features far away from the bacteria. Two bacteria, one prone and one diving head-first into the cell, may have entered using the same infection site.

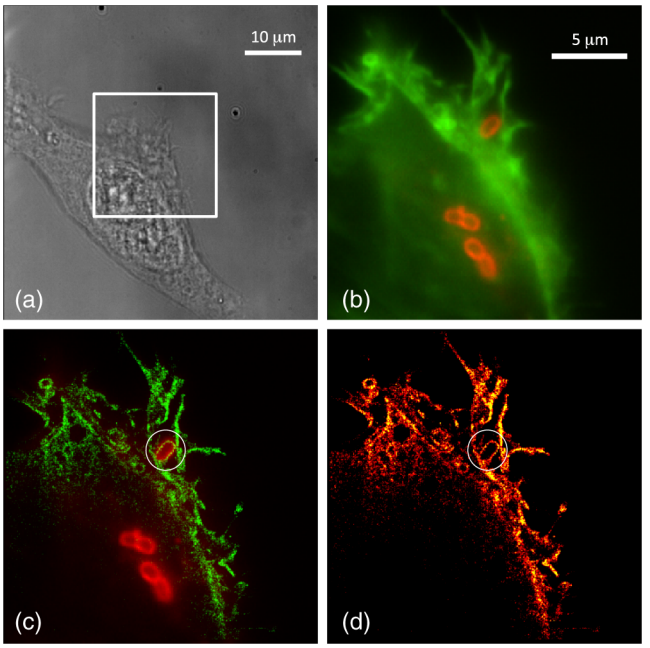

Fig. 5 (a) Changes to HeLa cells due to bacterial infection are visible with white light microscopy. (b) Merged image of *S. typhimurium* (red) and actin cytoskeleton (green) as observed by conventional epi-fluorescence microscopy. This region of interest corresponds to the box drawn in (a). (c) Merged single-molecule localization image of the *Salmonella* (red) and actin cytoskeleton (green). (d) Single-molecule localization image of the actin cytoskeleton without a *Salmonella* overlay shown in a flame scale. The ring of actin surrounding the bacteria is highlighted by a white circle in (c) and (d).

Interestingly, the bacterium closest to the cell membrane that has just entered the cell appears to be tightly coated in a ring of actin, whereas internalized bacteria lack this actin ring. A similar actin ring accompanying bacterial infection is shown in Fig. 3 [highlighted by arrows in Fig. 3(d)]. This ring of actin surrounding the internalized bacteria seems to appear sometime between 10 and 20 min postinfection since we did not observe an actin ring in recently internalized bacteria (5 min postinfection, Fig. 6). We note that this transitory actin ring formation around an invading bacteria appears different in nature from actin that associates with SCV >4 h postinfection.[17] Figure 7 shows a line scan across the actin ring circled in Fig. 4(d), with the full width at half maximum (FWHM) of this feature being ~100 nm. As our single-molecule localization precision for each molecule detected is typically 10 to 20 nm (limited primarily by noise rather than the total number of photons recorded),[12] this 100-nm FWHM closely represents the physical width of the actin bundle surrounding the bacteria. As a single F-actin mono (or thin) filament is ~60 Å in diameter, this ring structure is ~17 monofilaments wide.[36] Assuming a circular cross-section

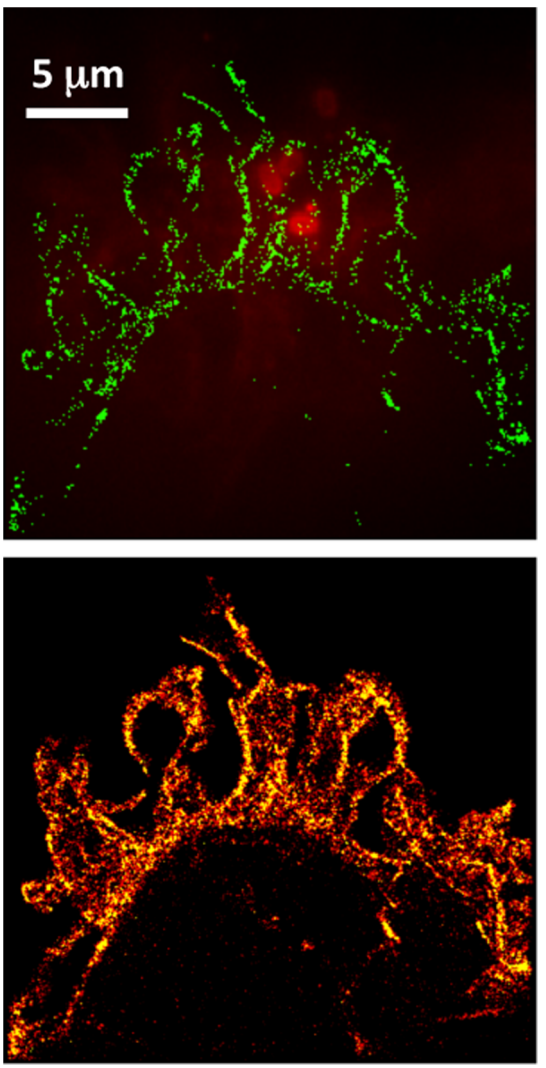

Fig. 6 Single-molecule localization images of actin restructuring 5 min postinfection at a multiplicity of infection of 40 to enhance the probability of internalization. While there are dramatic changes to the cytoskeleton, at this point internalized bacteria are not sheathed in a ring of actin.

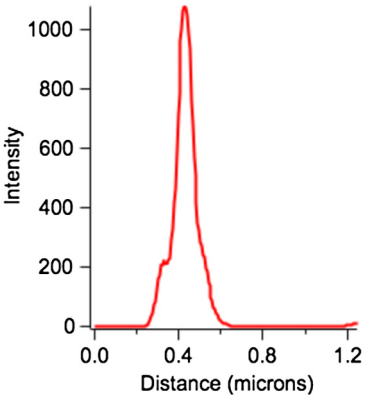

Fig. 7 Line scan across the actin ring circled in Fig. 5(d). The full width half maximum of this feature is ~100 nm.

for this ring structure, <280 monofilaments of actin comprise the actin ring surrounding the bacteria shown in Fig. 3(d).

4 Discussion and Conclusions

This work has demonstrated that new SMLM tools are compatible with imaging the early stages of bacterial infection. Benefits of SMLM include being able to directly visualize the number of actin fiber bundles comprising larger actin structures [e.g., Fig. 3(c)] as well as directly probe the number of actin monofilaments surrounding an invading bacteria [Figs. 5(d) and 7]. An interesting finding of this work was that internalized *Salmonella* can be encased in a thin (~100-nm wide) ring of actin, with this ring formation apparently being a transitory intermediate. These quantitative measures of the number and width of actin bundles restructured during bacterial infection lay the groundwork for estimating the energy needed and expended by the host cell during bacterial entry.

Both rings and cages of actin can be formed *ex vivo* inside giant unilamelar vesicles with the addition of α-actin or filamin.[37] We point out that α-actin is a key player in the formation of actin comet tails, which are important structures driving the internalization of different bacteria, including *Listeria*, into host cells during infection. A possible explanation for the observed actin ring formation is that bacterial effectors (such as SopE) that modulate Rho-GTPases[25] and restructure the cytoskeleton for bacterial internalization can induce nucleation of filamentous actin to levels needed for spontaneous actin ring formation inside or around internalized vesicles and vacuoles. We emphasize that a number of actin ring-like structures seen in Fig. 3(d) are not associated with an invading bacteria, raising the question of whether ring formation around the *Salmonella* is an obligatory intermediate in bacterial internalization or simply a result of the large amount of actin restructuring that occurs during infection.

Demonstrating the compatibility of SMLM with bacterial infection conditions lays the foundation for many avenues of future research. One future research path lies in multicolor SR imaging[38] (in 2-D or 3-D[13]) to correlate changes in the actin cytoskeleton with both bacterial effectors (such as SopE) and host proteins (such as Rac), which are important modulators of host cytoskeletal dynamics. In particular, our assumption of a circular cross-section for the actin ring that sometimes accompanies bacterial infection is marginally within the Z-resolution of cylindrical lens-based methods of 3-D localization of single molecules[13,39,40] and within the Z-resolution of interferometric techniques[34] and could conceivably be directly explored by these methods. Another potential avenue of future research is to use SR microscopy to visualize and quantify the spatial organization of host cell receptors that are known to aggregate in response to *Salmonella* infection.[23] Dynamic changes in the host cytoskeleton during infection, combined with confocal-based 3-D tracking of bacterial internalization,[41–43] also are within the temporal resolution of real-time single-molecule-based localization microscopy using compressed sensing techniques.[44]

Acknowledgments

This work was supported by the Los Alamos National Laboratory Directed Research and Development (LDRD) program and was in part performed at the Center for Integrated Nanotechnologies, a U.S. Department of Energy, Office of Basic Energy Sciences user facility at Los Alamos National Laboratory (Contract DE-AC52-06NA25396).

References

1. E. Betzig et al., "Imaging intracellular fluorescent proteins at nanometer resolution," *Science* **313**(5793), 1642–1645 (2006).
2. S. T. Hess, T. P. Girirajan, and M. D. Mason, "Ultra-high resolution imaging by fluorescence photoactivation localization microscopy," *Biophys. J.* **91**(11), 4258–4272 (2006).
3. M. J. Rust, M. Bates, and X. Zhuang, "Sub-diffraction-limit imaging by stochastic optical reconstruction microscopy (STORM)," *Nat. Methods* **3**(10), 793–796 (2006).
4. S. W. Hell and J. Wichmann, "Breaking the diffraction resolution limit by stimulated emission: stimulated-emission-depletion fluorescence microscopy," *Opt. Lett.* **19**(11), 780–782 (1994).
5. M. G. Gustafsson, "Surpassing the lateral resolution limit by a factor of two using structured illumination microscopy," *J. Microsc.* **198**(2), 82–87 (2000).
6. J. J. Han, A. P. Shreve, and J. H. Werner, "Super-resolution microscopy," in *Characterization of Materials*, E. N. Kaufmann, Ed., pp. 1026–1040, Wiley, New York (2012).
7. A. McEvoy et al., "Q&A: single-molecule localization microscopy for biological imaging," *BMC Biol.* **8**(1), 106 (2010).
8. S. W. Hell, *Single Molecule Spectroscopy in Chemistry, Physics and Biology*, pp. 365–398, Springer, Heidelberg, Germany (2010).
9. V. Westphal et al., "Video-rate far-field optical nanoscopy dissects synaptic vesicle movement," *Science* **320**(5873), 246–249 (2008).
10. L. Schermelleh et al., "Subdiffraction multicolor imaging of the nuclear periphery with 3D structured illumination microscopy," *Science* **320**(5881), 1332–1336 (2008).
11. M. Heilemann et al., "Subdiffraction–resolution fluorescence imaging with conventional fluorescent probes," *Angew. Chem. Int. Ed.* **47**(33), 6172–6176 (2008).
12. R. E. Thompson, D. R. Larson, and W. W. Webb, "Precise nanometer localization analysis for individual fluorescent probes," *Biophys. J.* **82**(5), 2775–2783 (2002).
13. B. Huang et al., "Whole-cell 3D STORM reveals interactions between cellular structures with nanometer-scale resolution," *Nat. Methods* **5**(12), 1047–1052 (2008).
14. K. Xu, H. P. Babcock, and X. Zhuang, "Dual-objective STORM reveals three-dimensional filament organization in the actin cytoskeleton," *Nat. Methods* **9**, 185–188 (2012).
15. W. Ip and D. A. Fischman, "High resolution scanning electron microscopy of isolated and in situ cytoskeletal elements," *J. Cell Biol.* **83**(1), 249–254 (1979).
16. S. Gruenheid and B. B. Finlay, "Microbial pathogenesis and cytoskeletal function," *Nature* **422**(6933), 775–781 (2003).
17. B. Finlay, S. Ruschkowski, and S. Dedhar, "Cytoskeletal rearrangements accompanying Salmonella entry into epithelial cells," *J. Cell Sci.* **99**(2), 283–296 (1991).

18. T. D. Pollard and G. G. Borisy, "Cellular motility driven by assembly and disassembly of actin filaments," *Cell* **112**(4), 453–465 (2003).
19. C. Dos Remedios et al., "Actin binding proteins: regulation of cytoskeletal microfilaments," *Physiol. Rev.* **83**(2), 433–473 (2003).
20. T. Kubori et al., "Supramolecular structure of the Salmonella Typhimurium type III protein secretion system," *Science* **280**(5363), 602–605 (1998).
21. S. B. Van Engelenburg and A. E. Palmer, "Imaging type-III secretion reveals dynamics and spatial segregation of Salmonella effectors," *Nat. Methods* **7**(4), 325–330 (2010).
22. J. E. Galan and R. Curtiss, "Cloning and molecular characterization of genes whose products allow Salmonella Typhimurium to penetrate tissue culture cells," *Proc. Natl. Acad. Sci.* **86**(16), 6383–6387 (1989).
23. F. Garcia-del Portillo et al., "Salmonella typhimurium induces selective aggregation and internalization of host cell surface proteins during invasion of epithelial cells," *J. Cell Sci.* **107**(7), 2005–2020 (1994).
24. D. Zhou and J. Galán, "Salmonella entry into host cells: the work in concert of type III secreted effector proteins," *Microbes Infect.* **3**(14), 1293–1298 (2001).
25. K. Aktories, "Bacterial protein toxins that modify host regulatory GTPases," *Nat. Rev. Microbiol.* **9**(7), 487–498 (2011).
26. K. T. Ly and J. E. Casanova, "Mechanisms of Salmonella entry into host cells," *Cell. Microbiol.* **9**(9), 2103–2111 (2007).
27. P. Cossart and P. J. Sansonetti, "Bacterial invasion: the paradigms of enteroinvasive pathogens," *Science* **304**, 242–248 (2004).
28. M. C. Schlumberger et al., "Real-time imaging of type III secretion: Salmonella sipa injection into host cells," *Proc. Natl. Acad. Sci. U. S. A.* **102**(35), 12548–12553 (2005).
29. D. Zhou, M. S. Mooseker, and J. E. Galán, "Role of the S. Typhimurium actin-binding protein sipa in bacterial internalization," *Science* **283**(5410), 2092–2095 (1999).
30. J. E. Galán and D. Zhou, "Striking a balance: modulation of the actin cytoskeleton by Salmonella," *Proc. Natl. Acad. Sci. U. S. A.* **97**(16), 8754–8761 (2000).
31. M. Tokunaga, N. Imamoto, and K. Sakata-Sogawa, "Highly inclined thin illumination enables clear single-molecule imaging in cells," *Nat. Methods* **5**(2), 159–161 (2008).
32. K. I. Mortensen et al., "Optimized localization analysis for single-molecule tracking and super-resolution microscopy," *Nat. Methods* **7**(5), 377–381 (2010).
33. C. S. Smith et al., "Fast, single-molecule localization that achieves theoretically minimum uncertainty," *Nat. Methods* **7**(5), 373–375 (2010).
34. G. Shtengel et al., "Interferometric fluorescent super-resolution microscopy resolves 3D cellular ultrastructure," *Proc. Natl. Acad. Sci.* **106**(9), 3125–3130 (2009).
35. T. Funatsu et al., "Imaging of single fluorescent molecules and individual ATP turnovers by single myosin molecules in aqueous solution," *Nature* **374**(6522), 555–559 (1995).
36. L. Stryer, *Biochemistry*, W.H. Freeman & Company, New York (1995).
37. L. Limozin and E. Sackmann, "Polymorphism of cross-linked actin networks in giant vesicles," *Phys. Rev. Lett.* **89**(16), 168103 (2002).
38. M. Bates et al., "Multicolor super-resolution imaging with photo-switchable fluorescent probes," *Science* **317**(5845), 1749–1753 (2007).
39. H. P. Kao and A. Verkman, "Tracking of single fluorescent particles in three dimensions: use of cylindrical optics to encode particle position," *Biophys. J.* **67**(3), 1291–1300 (1994).
40. G. J. Schütz et al., "3 D imaging of individual ion channels in live cells at 40 nm resolution," *Single Mol.* **1**(1), 25–31 (2000).
41. G. A. Lessard, P. M. Goodwin, and J. H. Werner, "Three dimensional tracking of individual quantum dots," *Appl. Phys. Lett.* **91**(22), 224106 (2007).
42. N. P. Wells et al., "Time-resolved three-dimensional molecular tracking in live cells," *Nano Lett.* **10**(11), 4732–4737 (2010).
43. J. J. Han et al., "Time-resolved, confocal single molecule tracking of individual organic dyes and fluorescent proteins in three dimensions," *ACS Nano* **6**(19), 8922–8932 (2012).
44. L. Zhu et al., "Faster STORM using compressed sensing," *Nat. Methods* **9**(7), 721–723 (2012).

Jason J. Han received his bachelor's degree in chemistry from Humboldt State University and his PhD in materials and physical chemistry from Washington State University. He currently serves as the director of the Electron and Optical Core Microscopy Facility at McLean Hospital of Harvard Medical School. His research interests include optical instrumentation development, single molecule and super-resolution imaging, electron microscopy, and applications in biophysics, nanotechnology, neurosciences, and national security and defense.

Yuliya A. Kunde: Biography is not available.

Elizabeth Hong Geller received her BA in biochemistry from Columbia University, New York City, in 1991. She then went to graduate school at MIT and got her PhD in cell and molecular biology in 1997. She spent three years at Cornell University as a postdoctoral fellow before coming to Los Alamos in 2000. At Los Alamos, she has worked on a variety of projects focused on pathogen virulence and host response and immunity.

James H. Werner is a technical staff member in the Center for Integrated Nanotechnologies of Los Alamos National Laboratory. He received his BS in applied physics from Caltech in 1992 and his PhD in applied physics from Cornell University in 1998, where he was a Hertz Foundation fellow. His research interests include biophysics, instrument development, laser spectroscopy, nanoscience, and analytic applications of single molecule detection by laser induced fluorescence.